Bioactive Materials 6 (2021) 490–502

Contents lists available at ScienceDirect

Bioactive Materials

journal homepage: http://www.keaipublishing.com/biomat

Accelerated degradation of HAP/PLLA bone scaffold by PGA blending facilitates bioactivity and osteoconductivity

Cijun Shuai[a,b,c], Wenjing Yang[a,b], Pei Feng[a,*], Shuping Peng[d,e], Hao Pan[f]

[a] State Key Laboratory of High Performance Complex Manufacturing, College of Mechanical and Electrical Engineering, Central South University, Changsha, 410083, China
[b] Institute of Bioadditive Manufacturing, Jiangxi University of Science and Technology, Nanchang, 330013, China
[c] Shenzhen Institute of Information Technology, Shenzhen, 518172, China
[d] NHC Key Laboratory of Carcinogenesis, School of Basic Medical Science, Central South University, Changsha, Hunan, 410013, China
[e] School of Energy and Machinery Engineering, Jiangxi University of Science and Technology, Nanchang, 330013, China
[f] Department of Periodontics & Oral Mucosal Section, Xiangya Stomatological Hospital, Central South University, Changsha, 410013, China

ARTICLE INFO

Keywords:
PGA
HAP/PLLA
Scaffold
Degradation
Bone regeneration

ABSTRACT

The incorporation of hydroxyapatite (HAP) into poly-L-lactic acid (PLLA) matrix serving as bone scaffold is expected to exhibit bioactivity and osteoconductivity to those of the living bone. While too low degradation rate of HAP/PLLA scaffold hinders the activity because the embedded HAP in the PLLA matrix is difficult to contact and exchange ions with body fluid. In this study, biodegradable polymer poly (glycolic acid) (PGA) was blended into the HAP/PLLA scaffold fabricated by laser 3D printing to accelerate the degradation. The results indicated that the incorporation of PGA enhanced the degradation rate of scaffold as indicated by the weight loss increasing from 3.3% to 25.0% after immersion for 28 days, owing to the degradation of high hydrophilic PGA and the subsequent accelerated hydrolysis of PLLA chains. Moreover, a lot of pores produced by the degradation of the scaffold promoted the exposure of HAP from the matrix, which not only activated the deposition of bone like apatite on scaffold but also accelerated apatite growth. Cytocompatibility tests exhibited a good osteoblast adhesion, spreading and proliferation, suggesting the scaffold provided a suitable environment for cell cultivation. Furthermore, the scaffold displayed excellent bone defect repair capacity with the formation of abundant new bone tissue and blood vessel tissue, and both ends of defect region were bridged after 8 weeks of implantation.

1. Introduction

Biopolymer/bioceramic composites have attracted increasing attention for their use as scaffold materials in bone tissue engineering because they might combine good processability of biopolymer with excellent bioactivity of bioceramic [1–3]. Among various biopolymer materials, poly-L-lactic acid (PLLA) is one of the promising materials because of its good biocompatibility and biodegradability [4–6]. It can degrade by nonenzymatic hydrolysis of ester bond into lactic acid, which is a natural intermediate in carbohydrate metabolism and can be eventually degraded into carbon dioxide and water. Besides, PLLA has been approved by the Food and Drug Administration (FDA) for clinical use in human and can be easily processed into porous scaffold with customized shape. Hydroxyapatite (HAP), a well-known bioceramic, has been extensively used in the replacement and regeneration of bone material because it not only has chemical composition similarity to the inorganic component of natural bone, but also exhibits outstanding biocompatibility, bioactivity and osteoconductivity [7,8]. Therefore, the combination of HAP with PLLA might endow scaffold with both the excellent bioactivity and osteoconductivity of HAP and good processibility and biodegradability of PLLA.

In order for HAP to exert its bioactivity and osteoconductivity, the presence of bone like apatite layer on HAP surface is crucial after implanted in vivo as it can form a bone-bonding between implant and living bone tissue [9,10]. It has been reported that the bone like apatite layer can provide a suitable substrate for osteoblastic growth, proliferation and differentiation, and this layer together with living cells forms new bone [11,12]. The first step for bone like apatite layer formation is the direct contact between HAP and body fluid, which then initiates ion exchange reaction. However, most of the HAP particles are

Peer review under responsibility of KeAi Communications Co., Ltd.
* Corresponding author.
E-mail address: fengpei@csu.edu.cn (P. Feng).

https://doi.org/10.1016/j.bioactmat.2020.09.001
Received 6 June 2020; Received in revised form 29 August 2020; Accepted 1 September 2020

embedded in the PLLA matrix for the HAP/PLLA composite scaffold. Moreover, PLLA displays very slow degradation rate ranging from 6 months to 3 years for complete degradation due to the hydrophobic methyl group in its backbone [13,14], which acts as a physical barrier inhibiting the contact between the HAP particles and body fluid. Therefore, how to accelerate the degradation rate of HAP/PLLA composite scaffold so that the HAP particles can be exposed from the PLLA matrix to body fluid is an urgent problem to be solved.

Some strategies including grafting and copolymerization techniques have been adopted for improving the degradation rate of PLLA to accelerate the degradation of HAP/PLLA composite scaffold [15–18]. Nugroho et al. [15] grafted polymer monomer acrylic acid (AA) on the surface of PLLA, and found that the grafted polymer chains could induce a local acidic environment, which in turn catalyzed the degradation of PLLA. Liu et al. [16] synthesized poly (hydroxyalkyl (meth)acrylate)-graft-poly (L-lactic acid) (PHAA-g-PLLA) copolymer by ring-opening polymerization of LLA and HAA, and the results indicated that the degradation rate of the copolymer was substantially accelerated than that of PLLA because the introduction of hydroxyl groups into polymer chain allows easy access to water molecules. While these methods may require more complex conditions and are difficult to control. Blending other biodegradable polymers with fast degradation rate has been widely used as a simple and effective way to improve the degradation rate [19,20]. Among the biodegradable polymers, poly (glycolic acid) (PGA) is a FDA-approved polymer with a relatively fast degradation rate [21]. The degradation rate of PGA is typically a few weeks for complete degradation due to its strong hydrophilicity [22,23]. PGA might degrade rapidly and produce a lot of pores in the polymer matrix when the HAP/PGA/PLLA scaffold is immersed in the body fluid environment, which will be beneficial to the exposure of HAP from matrix. Besides, the pores can increase the contact area between PLLA matrix and body fluid, thereby accelerating PLLA degradation.

In this work, PGA was incorporated into the HAP/PLLA scaffold to accelerate degradation so that the bioactivity and osteoconductivity of HAP could be fully displayed. And the composite scaffolds based on PGA, PLLA and HAP were fabricated by laser 3D printing technology. The effect of PLLA/PGA ratio on the hydrophilicity (including water absorption and water contact angle) and degradability (surface morphology change, weight loss and pH variation) of the scaffolds were investigated. The bioactivity was assessed by detecting bone like apatite layer formation from simulated body fluid (SBF) immersion tests and the cytocompatibility was analyzed by studying cell adhesion, spreading and proliferation in cell culture experiments. The bone regeneration ability of the scaffolds was evaluated by radiographic, micro-CT and histological analysis using rabbit radius defect mode.

2. Materials and methods

2.1. Materials

PLLA (M_w = 150,000, average particle size: 25–75 μm) and PGA (M_w = 100,000, average particle size: 5–20 μm) powder were purchased from Shenzhen Polymtek Biomaterial Co., Ltd (Shenzhen, China). HAP nanoparticles (average particle size: 20 nm in width and 150 nm in length) were purchased from Nanjing Emperor Nano Material Co., Ltd. (Nanjing, China). Phosphate buffered saline (PBS) and fetal bovine serum (FBS) solution were obtained from Cellgro-Mediatech Inc. Dulbecco's Modifed Eagle's Medium (DMEM), penicillin/streptomycin, simulated body fluid (SBF), calcein acetoxymethylester (calcein AM) and propidium iodide (PI) were purchased from Sigma-Aldrich.

2.2. Preparation of composite scaffold

Composite scaffolds were prepared with varying PLLA and PGA content and keeping the amount of HAP constant at 10 wt% as listed in Table 1 via laser 3D printing technology as described previously [24,25]. Our previous study indicated that the content of bioceramic phase beyond 12.5 wt% would result in poor mechanical properties [26]. Taking 1PLLA/1PGA/HAP scaffold as an example, the detailed preparation was described as follows: 4.5 g of PLLA powder and 4.5 g of PGA powder were mixed together with distilled water, and then the mixture was stirred and sonicated at 37 °C for 30 min. At the same time, 1.0 g of HAP powder was added into distilled water, and the solution was subjected to ultrasound and stirred for 30 min to reach a uniform suspension. The mixture suspension was obtained by adding the HAP suspension into the PLLA/PGA suspension and continuously sonicated for another 30 min. Thereafter, the suspension was centrifuged and the composite powder was obtained by drying at 37 °C for 24 h. Finally, the composite powder was spread on the build platform of laser 3D printing system to prepare composite scaffold by layer by layer processing. The processing parameters were optimized as: laser power of 2.2 W, scanning speed of 120 mm/min, spot diameter of 300 μm, layer thickness of 0.15 mm and scanning distance of 1.0 mm. The other types of scaffolds were prepared by varying compositions of PLLA and PGA according to the above procedure.

Table 1
Composition of the composite scaffolds.

Label	Scaffold	PLLA (wt%)	PGA (wt%)	HAP (wt%)
1#	PLLA/HAP	90	0	10
2#	3PLLA/1PGA/HAP	67.5	22.5	10
3#	1PLLA/1PGA/HAP	45	45	10
4#	1PLLA/3PGA/HAP	22.5	67.5	10
5#	PGA/HAP	0	90	10

2.3. Physical and chemical characterization

Surface morphologies of composite powder and scaffolds were investigated using a scanning electron microscope (SEM, Phenom ProX desktop SEM, Phenom World, Netherlands) after the specimens were sputter coated with gold-palladium. The elements composition and distribution were analyzed with an energy dispersive X-ray spectroscopy (EDS) attached to the SEM. Phase composition of the composite scaffolds was recorded using an X-ray diffraction (XRD, D8 Advance, German Bruker Co., German) in the 2θ range of 10°–50° with scan speed of 8°/min. For the analysis, thin film samples were prepared in size of 1 cm × 1 cm and coated on glass substrates. Chemical characteristics were carried out using a Fourier transform infrared spectroscopy (FTIR, NicoletteTM 6700, Thermo Electron Corp., USA) in the 500-4000 cm^{-1} range.

Thermal analysis including differential scanning calorimeter (DSC) and thermogravimetric analysis (TGA) were carried out using a synchronous thermal analyzer (Nanjing Dazhan institute of electromechanical technology, China) in nitrogen atmosphere at a heating rate of 10 °C/min. Specimens (about 8 mg) enclosed in aluminum pans were heated from 50 to 500 °C. Compressive properties including compressive strength and modulus of the scaffolds were tested using an universal testing machine (Shanghai Zhuoji Instruments Co., Ltd, China) in ambient atmospheric condition at a strain rate of 0.5 mm/min. The specimens were cylinders (13 mm in diameter and 15 mm in thickness), and the compressive modulus were obtained from the initial slope of the stress-strain curve. Five specimens were tested for each type and the average results were recorded.

Water absorption capacity was determined after immersion of preweighted cylindrical scaffold in 10 ml water at 37 °C for 24 h. Then the scaffold specimens were wiped with filter paper to remove surface liquid, and the wet weights of the specimens were recorded. The water absorption was calculated by the following equation [27]: water absorption $=(M_w\text{-}M_{dry})/M_d \times 100\%$, where M_w and M_d were the wet and

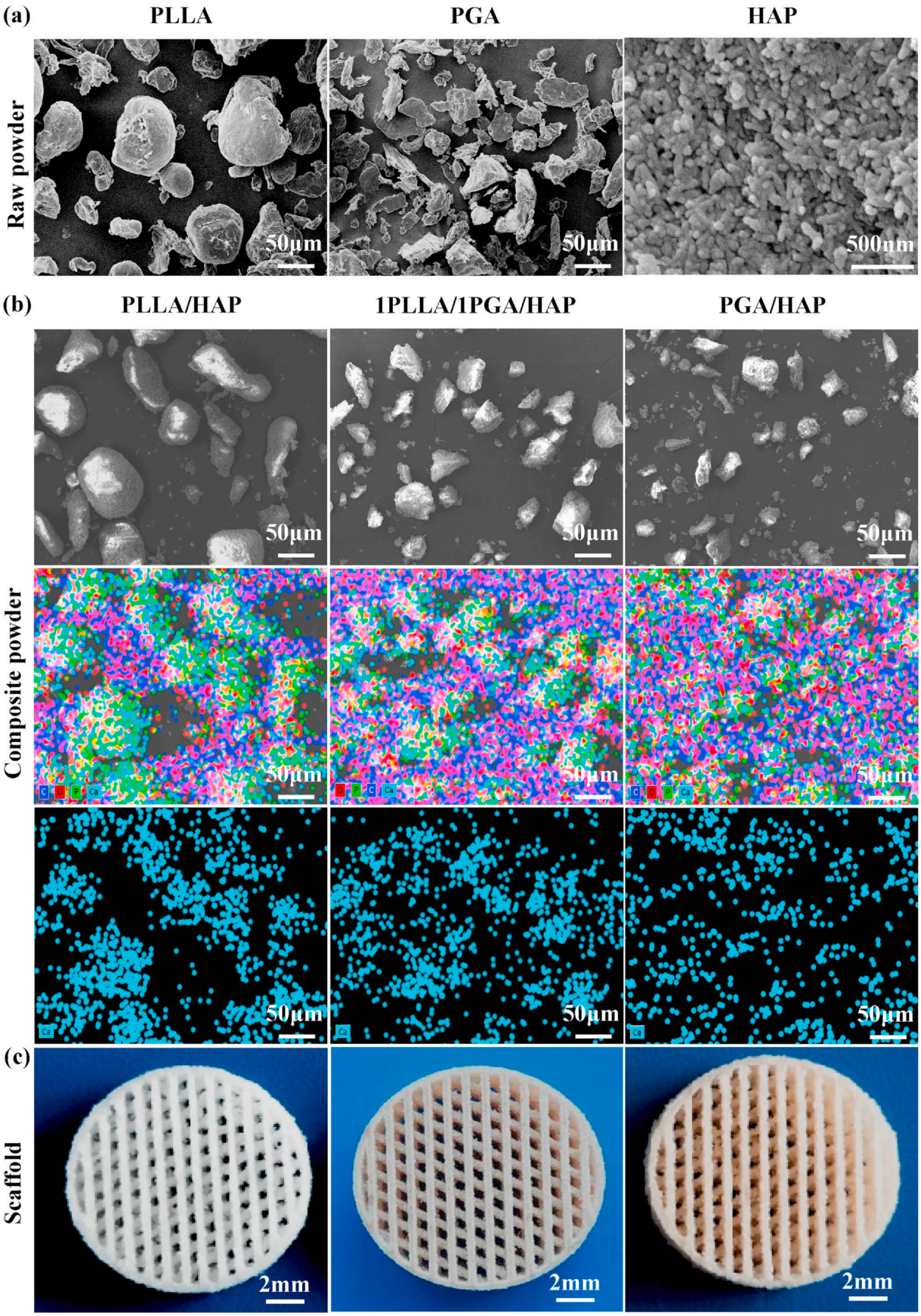

Fig. 1. (a) Raw powder of PLLA, PGA and HAP, (b) SEM micrographs and the corresponding EDS elemental mapping images of the prepared PLLA/HAP, 1PLLA/1PGA/HAP and PGA/HAP composite powder, (c) Typical optical images of the PLLA/HAP, 1PLLA/1PGA/HAP and PGA/HAP scaffolds seen from the top.

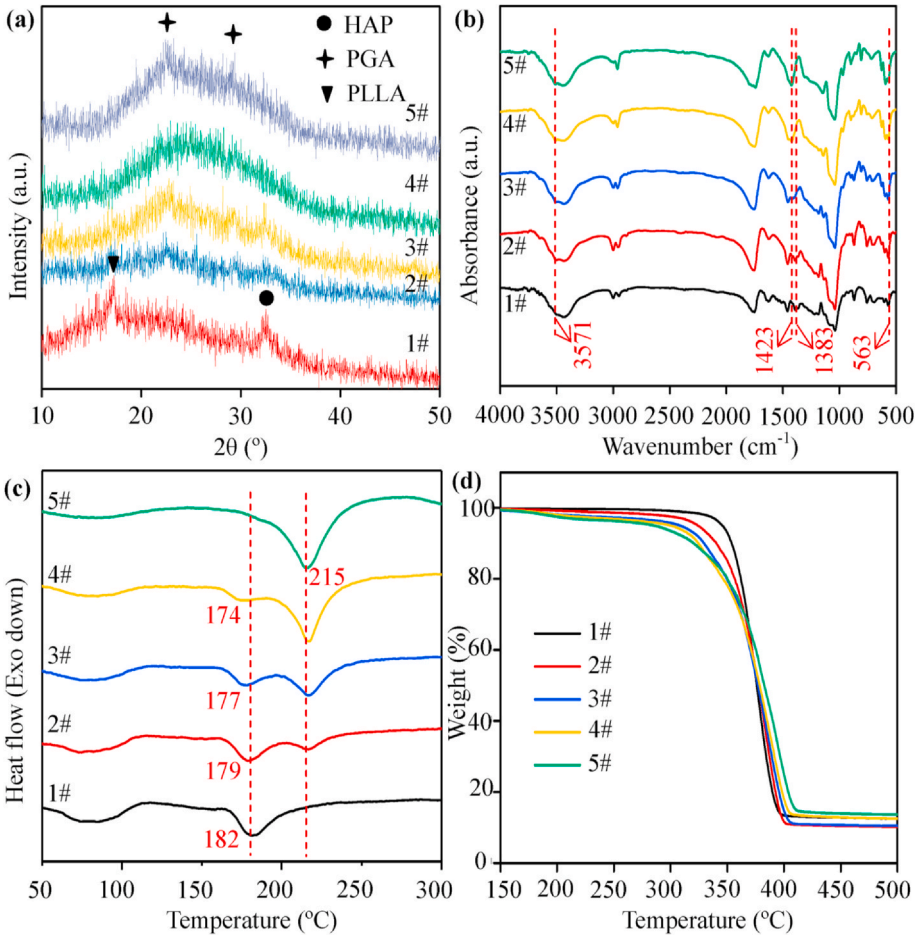

Fig. 2. (a) XRD patterns, (b) FTIR spectra, (c) DSC and (d) TGA curves of the composite scaffolds. 1# represents the PLLA/HAP scaffold, 2# represents the 3PLLA/1PGA/HAP scaffold, 3# represents the 1PLLA/1PGA/HAP scaffold, 4# represents the 1PLLA/3PGA/HAP scaffold, 5# represents the PGA/HAP scaffold.

dry weights of scaffold specimens, respectively. Hydrophilicity of the scaffolds was qualitatively determined by measuring the water contact angle with distilled water using a Theta Optical Tensiometer (KSV instruments, Ltd., Finland). A drop of water dripped from syringe on scaffold specimens, and the drop shape on the specimen surface was recorded using a camera attached with system. The contact angle was detected from five different places and with three types of specimens.

2.4. Biodegradability and bioactivity of the scaffolds

Biodegradability of scaffolds was studied by immersing the specimens in PBS solution (pH = 7.4, 37 °C) for a period of 28 d by monitoring the weight loss, pH variation and morphology change. For the experiment, the scaffolds were cut to size (13 mm in diameter and 10 mm in thickness) and were prewetted with PBS to ensure permeation through the specimens. Each specimen was submerged in a 15-ml centrifuge tube that contained 10 ml PBS solution, and the tubes were maintained at 37 °C in an incubator. After being incubated for various time duration (7, 14, 21 and 28 d), the specimens were taken out from the solution, rinsed with distilled water, and dried in a vacuum oven at 40 °C for 12 h. The weight loss was calculated by the following equation [28]: weight loss $=(W_0\text{-}W_1)/W_0 \times 100\%$, where W_0 and W_t were the original weight and the weight of the specimen after immersing in PBS up to day t, respectively. The pH of the degradation solution was measured once 7 d for 28 d. The morphologies of the specimens after degradation at different time intervals were studied using SEM. Bioactivity was evaluated by immersing the scaffold specimens in SBF solution at 37 °C for various time duration (7, 14, 21 and 28 d). After the specified times, the specimens were removed, rinsed with distilled water to remove adsorbed minerals, and then dried in a vacuum oven at 40 °C for 12 h. Finally, the specimens were viewed and analyzed using SEM and EDS.

2.5. Cell culture of the scaffolds

Prior to cell seeding, scaffold specimens (13 mm in diameter and 15 mm in thickness) were processed using the following steps: (1) 70% ethanol for 30 min, (2) rinsed three times with PBS solution and exposed to UV light for sterilization, (3) incubated in cell culture medium for 30 min. MG-63 human osteoblast-like cells were used for cell seeding, and they were cultured and maintained in DMEM supplemented with 10% FBS and 1% penicillin/streptomycin at 37 °C in a humidified atmosphere of 5% CO_2. Cells were seeded on to the specimens at a concentration of 1×10^5 cells/ml and incubated in the culture medium for 1, 3, 5 and 7 d. The adhesion and spreading properties of MG-63 cells on the specimens were evaluated using SEM. Before observing, the specimens were fixed in 2.5% glutaraldehyde, sterilized with a series of gradient alcohol concentration, dried in a vacuum oven and sputter-coated with platinum.

For live/dead cell staining, cell morphologies on the specimens were visualized by staining with calcein AM and PI, which could label live cells and dead cells, respectively. The specimens were examined by using a fluorescence microscope (Olympus Corporation, Japan). The living cells were stained as green and the dead as red. Cell proliferation was evaluated using cell counting kit-8 (CCK-8, Sigma-Aldrich Co., USA) assay. At different predetermined time points, CCK-8 solution was

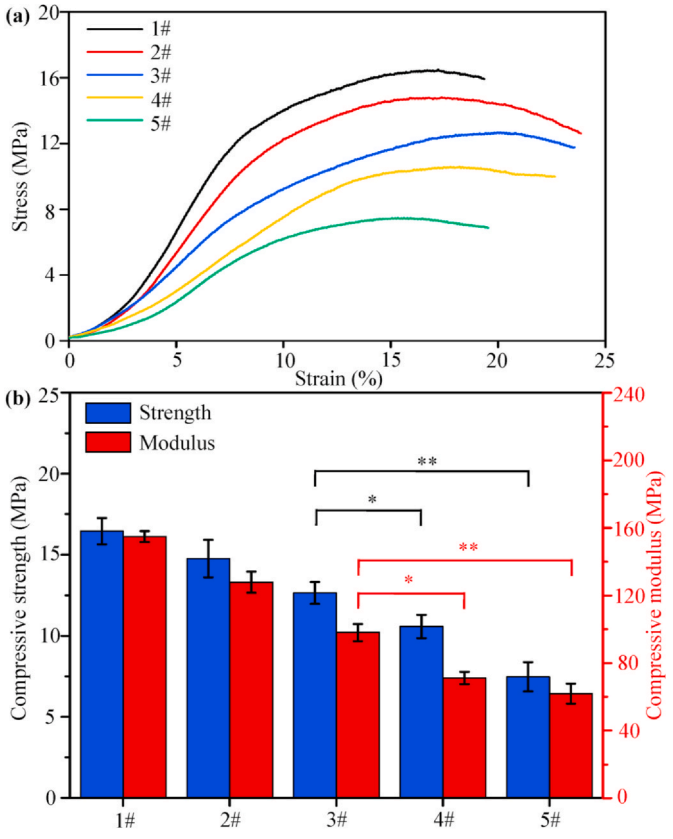

Fig. 3. (a) The typical stress-strain curves, (b) Compressive strength and modulus of the composite scaffolds (*$P < 0.05$ and **$P < 0.01$). 1# represents the PLLA/HAP scaffold, 2# represents the 3PLLA/1PGA/HAP scaffold, 3# represents the 1PLLA/1PGA/HAP scaffold, 4# represents the 1PLLA/3PGA/HAP scaffold, 5# represents the PGA/HAP scaffold. Data were presented as mean ± standard deviation.

introduced to each well and incubated for 4 h at 37 °C in a CO_2 incubator. The optical density (OD) value at 450 nm of the mixed solution was measured using a microplate reader.

2.6. In vivo animal experiments

Animal experiment was approved by the Institutional Animal Care and Use Committee at Xiangya Hospital of Central South University (Changsha, China). Eighteen New Zealand white rabbits aged five months weighting 2.5–3 kg were used for the animal experiment, and they were evenly divided into three groups. Considering the fact that the results obtained from mechanical and degradation properties tests, we selected the scaffold with the optimal overall performances for in vivo bone defect repair test. For the implantation surgery, the rabbits were administered anesthesia through intramuscular injection of sodium pentobarbital. Then, a 15 mm segmental defect was produced in rabbit radius using a reciprocating saw supplemented by copious irrigation with sterile saline solution. The segmental defects in first group were implanted with the 1PLLA/1PGA/HAP scaffold specimens (4 mm in diameter and 15 mm in thickness), and defects in second group were implanted with the PLLA/HAP scaffold specimens (4 mm in diameter and 15 mm in thickness). The defects in the third group were kept empty as control. The incision was sutured, and the incision was sutured layer by layer and disinfected with iodophor following surgery, and wrapped with gauze without applying external fixation. The animals were injected penicillin to prevent infection. Rabbits were euthanatized with overdose pentobarbital injection at 4 and 8 weeks post-implantation, and the harvested specimens were collected for histological examination.

X-ray and micro-CT analysis were performed to evaluate bone formation after surgery using an IVIS Lumina XR instrument (PerkinElmer, USA) and a micro-CT imaging system (SkyScan, Bruker, Belgium), respectively. After scanning, the defective radiuses were scanned and reconstructed by software, and the bone volume fraction and mineral density were calculated. The harvested specimens were fixed overnight in formaldehyde, dehydrated, embedded in paraffin, sectioned in 5 μm slices and then mounted on glass slides. After being stained with Hematoxylin and eosin (HE) and Masson trichrome (MT), the specimens were viewed under an optical microscope for histological observations.

2.7. Statistical analysis

Quantitative data were statistically analyzed to express as mean ± standard deviation. The results were analyzed using one way ANOVA to evaluate the statistical significance. The data was considered significant only if the $p < 0.05$, * indicates $p < 0.05$ and ** indicates $p < 0.01$.

3. Results and discussion

SEM images of the raw PLLA, PGA and HAP powder were shown in Fig. 1(a). The raw PLLA and PGA powder were irregular shape, and the HAP powder was needle shaped with a length of about 150 nm and a width of about 20 nm. The prepared composite powder was characterized by SEM and EDS analysis, and the porous scaffolds were imaged by digital camera. SEM micrographs and the corresponding EDS elemental mapping images of the prepared PLLA/HAP, 1PLLA/1PGA/HAP and PGA/HAP composite powder were shown in Fig. 1(b). It could be seen that some small particles were attached to the surface of the relatively large particles. The EDS elemental maps confirmed that Ca and P elements were mainly distributed in the relatively large particles. These indicated that the small particles were HAP nanoparticles, and they formed aggregates on the polymer particles due to the large specific surface area and high surface energy. Porous scaffolds with well-interconnected open-pore structure were successfully fabricated via laser 3D printing technology by controlling laser scanning distance and path, as shown in Fig. 1(c). Laser 3D printing technology, an additive manufacturing process, used a laser to sinter powder materials for producing parts with individual shape and complex internal pore structure [29,30]. It could fabricate smaller tissues by enabling drop-on-demand patterning of different types of cells and biomaterials on the same planar surface to enhance the cell-matrix interactions [31–33]. The pore size of the scaffolds was approximately 500 μm, and it had been reported that scaffold with a pore size ranging from 100 to 500 μm was beneficial to cell growth and osteoconductivity [34,35].

Phase structures and functional groups of the composite scaffolds were characterized by XRD patterns and FTIR spectra, respectively. The characteristic peak at around 17° in the XRD spectra could be ascribed to PLLA [36], as shown in Fig. 2(a). Two main characteristic peaks at around 22° and 29° corresponding to the (110) and (020) planes of the crystal structure were ascribed to PGA [20]. The characteristic peak of PLLA decreased in intensity whereas the characteristic peak of PGA increased as the content of PGA in the scaffolds increased. The peak could be ascribed to HAP with the major peak at around 32° corresponding to the (211) diffraction plane of crystalline HAP [37]. From the FTIR spectra in Fig. 2(b), the peaks at around 1752 cm^{-1} and 1038 cm^{-1} could be assigned to the -C=O stretching vibration and -C-C-O stretching vibration [38], respectively. The peak at around 1457 cm^{-1} corresponded to the $-CH_3$ bending vibration, and the peaks at around 2998 cm^{-1} and 2946 cm^{-1} corresponded to the $-CH_2$ stretching vibration [39]. The absorption peaks at around 3571 cm^{-1} and 563 cm^{-1} corresponded to the stretching vibration of $-OH^-$ and bending vibration of $-PO_4^{3-}$ [40], respectively. The characteristic peaks of $-PO_4^{3-}$ and $-OH^-$ belonging to HAP were presented in all the spectra of

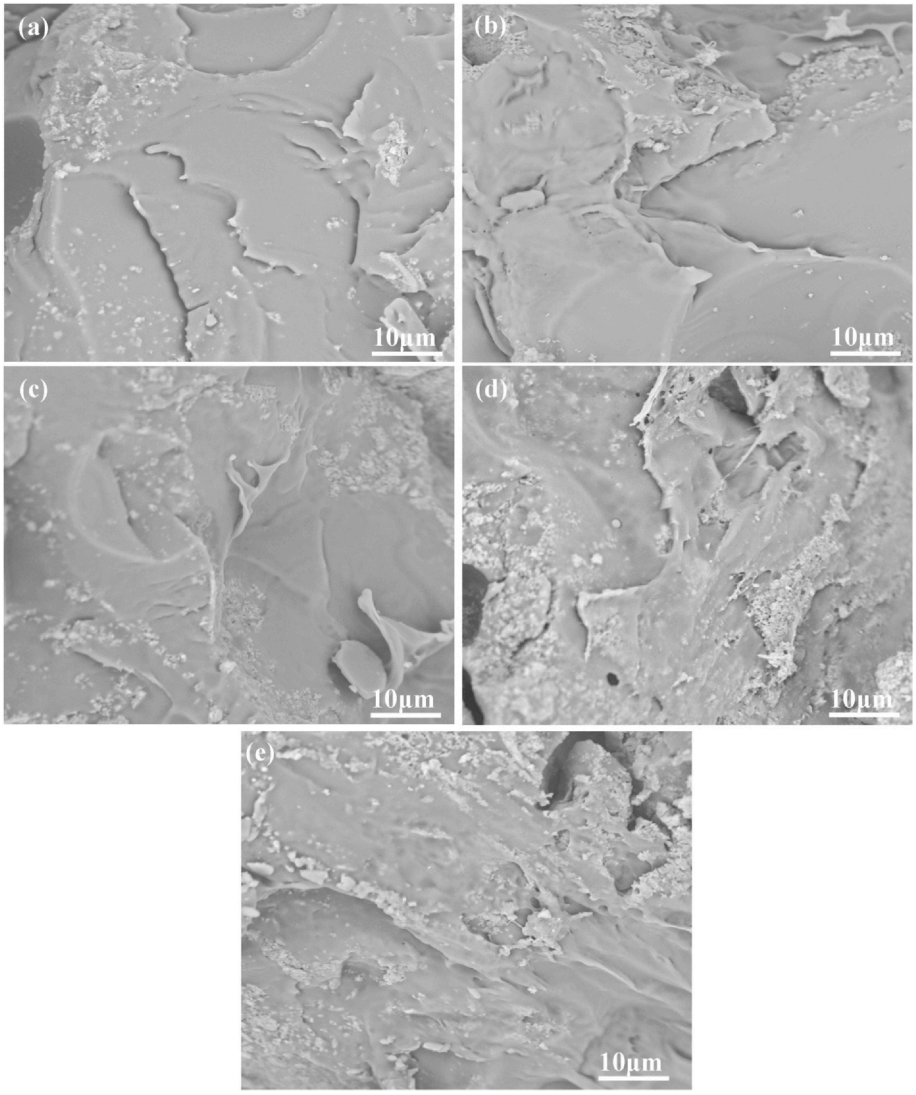

Fig. 4. SEM micrographs for fracture surface of the (a) PLLA/HAP scaffold, (b) 3PLLA/1PGA/HAP scaffold, (c) 1PLLA/1PGA/HAP scaffold, (d) 1PLLA/3PGA/HAP scaffold, (e) PGA/HAP scaffold.

composite scaffolds. The characteristic vibrations of the groups of PLLA and PGA occurred at around 1383 cm^{-1} ($-CH_3$) and 1423 cm^{-1} ($-CH_2$), respectively. The peak at around 1383 cm^{-1} disappeared while the peak at around 1423 cm^{-1} appeared as the content of PGA in the scaffolds increased.

Thermal properties of the composite scaffolds were investigated by DSC and TGA, and the results were presented in Fig. 2(c) and (d), respectively. The melting peaks of the PLLA/HAP and PGA/HAP scaffolds were observed at around 182 °C and 215 °C, respectively. For the 3PLLA/1PGA/HAP, 1PLLA/1PGA/HAP and 1PLLA/3PGA/HAP scaffolds, two melting peaks were observed in the DSC curves. The melting peak of PLLA became weak while the melting peak of PGA became strong as the content of PGA increased. When PGA content increased from 22.5% to 67.5%, the first melting peak of the scaffolds decreased from 179 °C to 174 °C, which indicated that the addition of PGA decreased the melting temperature of scaffolds. The reason was that the regularity of chain segment in the scaffolds decreased with the increase of PGA content, as a result, the chain structure became loose and chain mobility was enhanced. The thermogravimetric behavior of the composite scaffolds was almost the same from the TGA curves. The decomposition temperature at 5 wt% weight loss of the PLLA/HAP and PGA/HAP scaffolds were 345 °C and 286 °C, respectively. The initial decomposition temperature of the composite scaffolds decreased gradually with the increase of PGA content, indicating that the addition of PGA decreased the thermal stability. The residual weight ratio of the PLLA/HAP, 3PLLA/1PGA/HAP and 1PLLA/1PGA/HAP scaffolds were around 10%, which belonged to the residual weight of HAP. While the residual weight ratio of the 1PLLA/3PGA/HAP and PGA/HAP scaffolds was around 13%, which belonged to the residual weight of HAP and carbon.

Scaffold for bone defect repair should possessed good mechanical properties so that to provide enough support for cell and tissue [41]. In the present study, compressive properties of the composite scaffolds were examined. The typical stress-strain curves were illustrated in Fig. 3(a), as a function of PLLA/PGA rations. It could be seen that all the scaffolds exhibited a similar stress-strain behavior, and the increasing of PGA weight caused the decreasing of compressive properties. The compressive strength and modulus of the scaffolds were shown in Fig. 3(b). With regard to the PLLA/HAP scaffold, it displayed strong ability to resist deformation with the maximum strength and modulus high up to 16.6 ± 0.9 MPa and 155.3 ± 3.3 MPa, respectively. Conversely, the PGA/HAP scaffold possessed the lowest compressive strength and modulus. The compressive properties of other types of scaffolds were intermediated between the PLLA/HAP and PGA/HAP scaffolds, which exhibited a trend of decline with PGA content increasing. The strength and modulus of the 1PLLA/1PGA/HAP scaffold

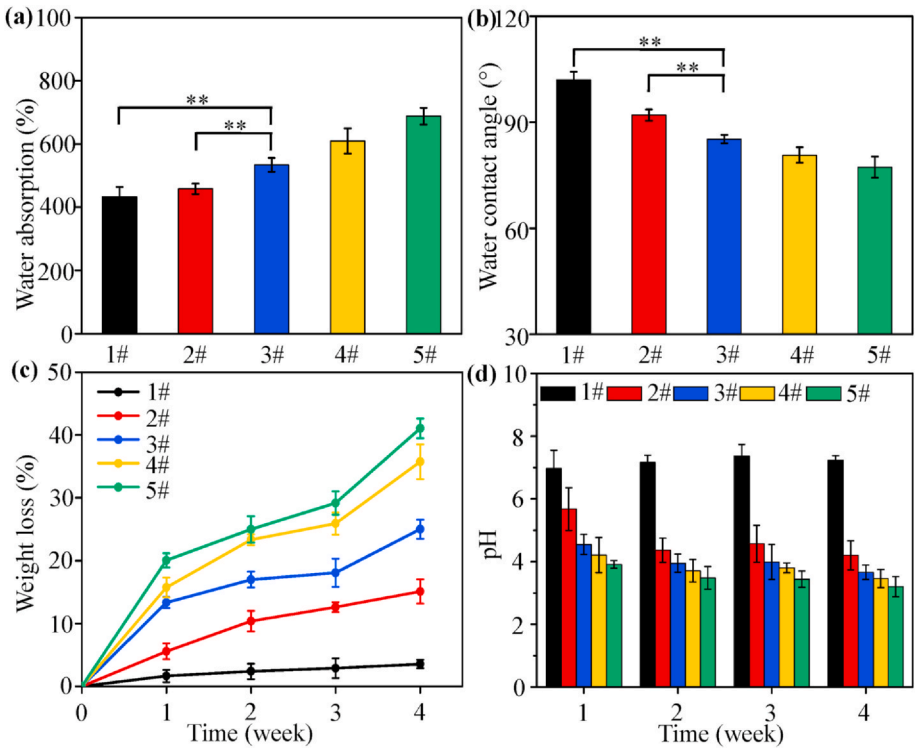

Fig. 5. (a) Water absorption and (b) water contact angle of the scaffolds (**$P < 0.01$), (c) Weight loss of the scaffolds and (d) pH of the solution. 1# represents the PLLA/HAP scaffold, 2# represents the 3PLLA/1PGA/HAP scaffold, 3# represents the 1PLLA/1PGA/HAP scaffold, 4# represents the 1PLLA/3PGA/HAP scaffold, 5# represents the PGA/HAP scaffold. Data were presented as mean ± standard deviation.

were 12.9 ± 0.8 MPa and 95.7 ± 5.2 MPa, respectively, which were higher than that of the 1PLLA/3PGA/HAP and PGA/HAP scaffolds (*$P < 0.05$ or **$P < 0.01$).

Fracture surface morphologies of the scaffold with different PLLA/PGA rations were observed by SEM, and the micrographs were shown in Fig. 4. The PLLA/HAP scaffold had a homogeneous and smooth fracture surface, which exhibited a typical brittle fracture behavior (Fig. 4a). The fracture surface exhibited much roughness and increased tough failure with the increase in mass fraction of PGA (Fig. 4b–d). The results indicated that the incorporation of PGA into PLLA could change the fracture mode from obvious brittle to tough fracture. There was no obvious interface in the polymer matrix, indicating that the good compatibility between PLLA and PGA. It was noted that the fracture surface of the PGA/HAP scaffold had some large plastic deformation, indicating a typical tough fracture behavior (Fig. 4e).

Water absorption was considered to be particularly important for bone scaffold, because it could reflect the efficiency of body fluid absorption and nutrient transport. It could be seen that the PLLA/HAP scaffold had the lowest water absorption whereas the PGA/HAP scaffold had the highest water absorption, as shown in Fig. 5(a). Previous studies indicated that PLLA was a relatively hydrophobic material with a very low water uptake [42], while PGA was relatively hydrophilic material with a very high water uptake [43]. The water absorption of the PLLA/PGA/HAP scaffolds changed with ratios of PLLA/PGA, and it increased with increasing content of PGA. The water absorption of the 1PLLA/1PGA/HAP scaffold was significantly higher than that of the PLLA/HAP and 3PLLA/1PGA/HAP scaffold (**$P < 0.01$). The variation of water absorption of the scaffolds was evaluated by measuring the water contact angle, and the results were presented in Fig. 5(b). The water contact angle of the scaffolds decreased with the increase in mass fraction of PGA, demonstrating an improved hydrophilicity of scaffolds. These results indicated that the water absorption and contact angle of the scaffold could be adjusted by changing the PLLA/PGA ratio.

Degradation properties of the composite scaffolds were assessed by weight loss, pH variation and morphological observation. Weight loss of the scaffolds after immersion in PBS solution was tested every 7 d to track the degradation rate for each scaffold type, and the results were presented in Fig. 5(c). Obviously, all the scaffolds lost mass over the time of degradation. The PLLA/HAP scaffold underwent the slowest degradation rate with only around 3.3 ± 2.6% weight loss. Aydin et al. [44] had indicated that PLLA composite fibers with 10% HAP in weight did not exhibit a significant weight loss during in vitro degradation studies. It was worth noting that the degradation rate of scaffold was greatly accelerated with the increase of PGA. Specifically, the 1PLLA/1PGA/HAP scaffold had 25.0 ± 4.2% weight loss, which was a little lower than that of the poly (D,L lactide-coglycolide (PLGA)/HAP scaffold or composite [45,46]. The results indicated that PGA regulated the degradation rate of scaffolds, which could be attributed to the fact that PGA's strong hydrophilicity leaded to self-degradation and increased the contact area between water molecules and PLLA chains, thus catalyzed the hydrolysis of PLLA. The pH of the solution after degradation was tested every 7 d, as shown in Fig. 5(d). It could be seen that the pH of the solution decreased rapidly from the initial value with the increase in mass fraction of PGA in the scaffolds. The decreasing in pH was attributed to the increase in lactic acid and glycolic acid from polymer hydrolysis. Particularly, the pH changed very little for the PLLA/HAP scaffold, which was similar to the reported PLLA/HAP fiber or PLLA/HAP scaffold [47,48].

The surface morphologies of scaffold before and after PBS immersion were showed in Fig. 6. Before PBS immersion, all the scaffolds exhibited a smooth and dense surface without any noticeable pore, crack and surface defect (Fig. 6a). After PBS immersion for 28 d, the surface morphologies of the composite scaffolds changed significantly. For the PLLA/HAP scaffold, some tiny pores were observed on the surface (Fig. 6b). The number of tiny pores increased, and some tiny pores became incorporated into larger pores with small amounts of defects for the 3PLLA/1PGA/HAP scaffold (Fig. 6c). The surface became rougher, and some cracks were observed for the 1PLLA/1PGA/HAP scaffold (Fig. 6d). The 1PLLA/3PGA/HAP and PGA/HAP scaffolds exhibited obvious degradation with increase of corrosion (Fig. 6e and f). It could be clearly seen that some HAP particles exposed from the polymer matrix after degradation, which would be beneficial to display the bioactivity and osteoconductivity of HAP. Our previous study indicated that the degradation of biopolymer could expose the wrapped

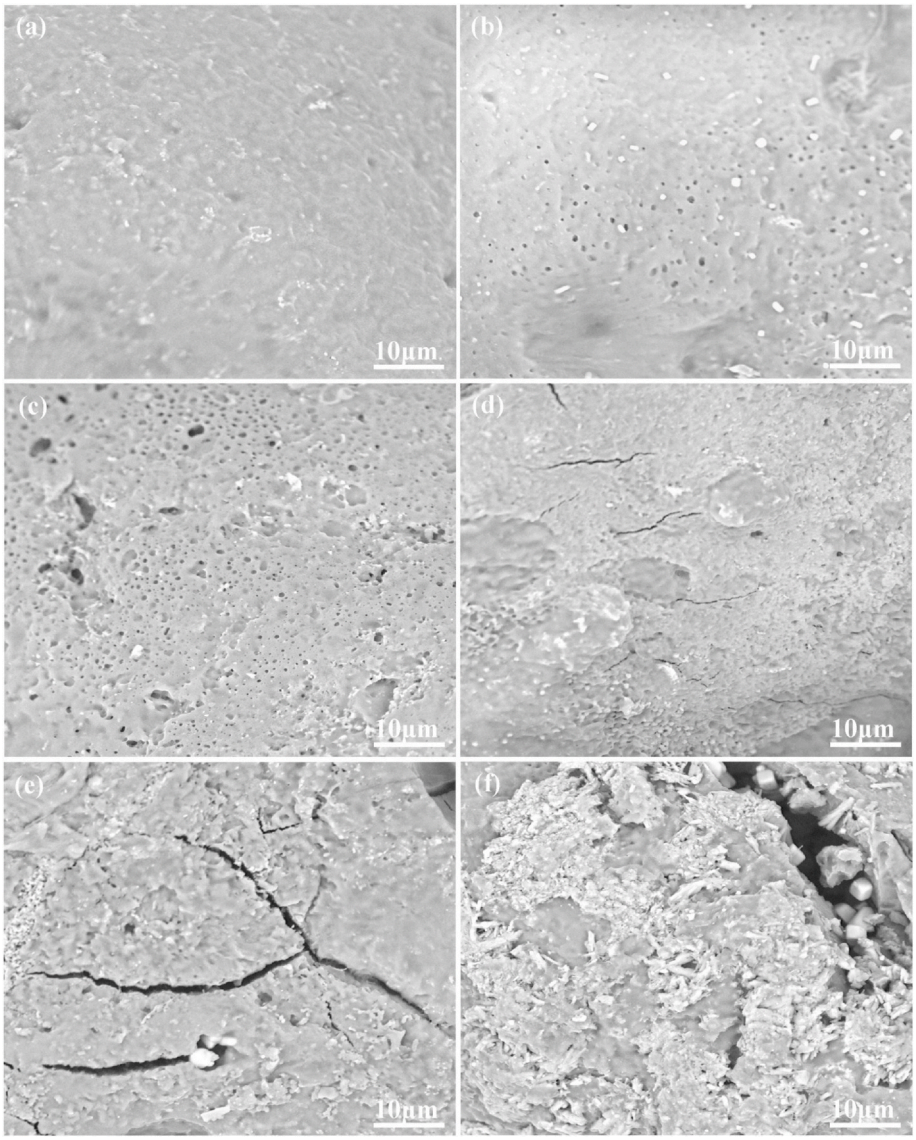

Fig. 6. SEM micrographs of surface morphologies of the 1PLLA/1PGA/HAP scaffold (a) before PBS immersion and (b–f) after PBS immersion for 28 d, (b) the PLLA/HAP scaffold, (c) the 3PLLA/1PGA/HAP scaffold, (d) the 1PLLA/1PGA/HAP scaffold, (e) the 1PLLA/3PGA/HAP scaffold, (f) the PGA/HAP scaffold.

bioceramic from polymer matrix to body fluid [49]. As a result, bioceramic could contact and exchange ion with body fluid.

Scaffold for bone regeneration must possessed the ability to form an apatite layer on its surface for bonding to living bone tissue upon implantation in the body [50]. The apatite layer formation ability of the composite scaffolds was assessed by soaking the specimens in SBF solution up to 28 d under normal physiological conditions. The SEM micrographs and the corresponding EDS spectra of the scaffolds after soaking in SBF were shown in Fig. 7. A large number of spherical particles deposited on the surface of the scaffolds from SEM observation. The amount of deposited particles increased obviously and formed a dense particle layer with the increase in mass fraction of PGA in the scaffolds. EDS results demonstrated that Ca and P element peaks in addition to C, O and Au peaks were detected within the composite scaffolds. The Ca/P ratio of the deposited particle layer increased from 1.56 to 1.67, which was near to that of HAP. These results indicated that all the scaffolds had the ability to induce bone like apatite layer formation, and more PGA content would be beneficial to apatite layer formation. Previous studies have indicated that the degradation and apatite formation of bioactivity materials in body fluid environment occurred simultaneously [51–53]. From the degradation experiment, it could be seen that the degradation rate of the scaffolds increased with the increase in mass fraction of PGA. The degradation of PGA produced a lot of pores in the matrix, resulting in the exposion of HAP from the matrix. And the produced pores could also increase the contact area between PLLA and body fluid which accelerated PLLA degradation and resulted in a further increase of the HAP exposion. When the exposed HAP contacted with body fluid, HAP would dissolve and release Ca^{2+} and PO_4^{3-}, which provided favorable sites for apatite nucleation and crystallization. The release of Ca^{2+} and PO_4^{3-} ions increased the local concentration around HAP particle surface and promoted surface nucleation. And then, OH^- and CO_3^{2-} were absorbed on HAP surface through electrostatic attraction and chemical bonding, thereby forming bone like apatite on the scaffold [54,55].

Based on the above mechanical properties, degradation properties and bioactivity analysis, the 1PLLA/1PGA/HAP scaffold exhibited moderate mechanical and degradation properties as well as good apatite layer formation ability. Therefore, the 1PLLA/1PGA/HAP scaffold was chosen for the following investigations including cytocompatibility and bone defect repair experiments since it possessed optimal comprehensive properties for cell growth and bone regeneration. Cell viability, adhesion and proliferation were important properties to display

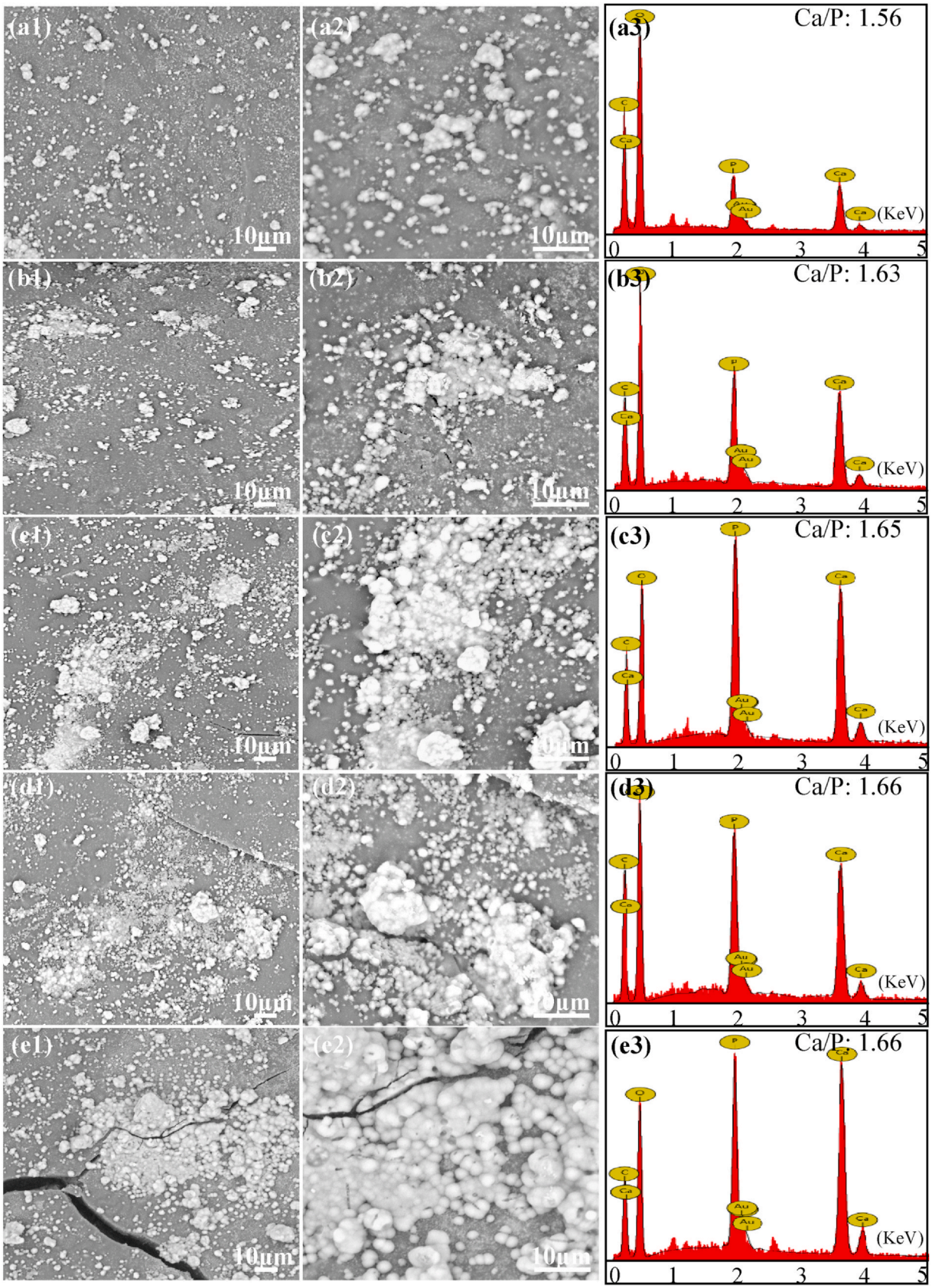

Fig. 7. SEM micrographs and the corresponding EDS spectra of the scaffolds (magnification × 2000, × 5000) incubated in SBF solution for 28 d (a1, a2, a3) the PLLA/HAP scaffold, (b1, b2, b3) the 3PLLA/1PGA/HAP scaffold, (c1, c2, c3) the 1PLLA/1PGA/HAP scaffold, (d1, d2, d3) the 1PLLA/3PGA/HAP scaffold, (e1, e2, e3) the PGA/HAP scaffold.

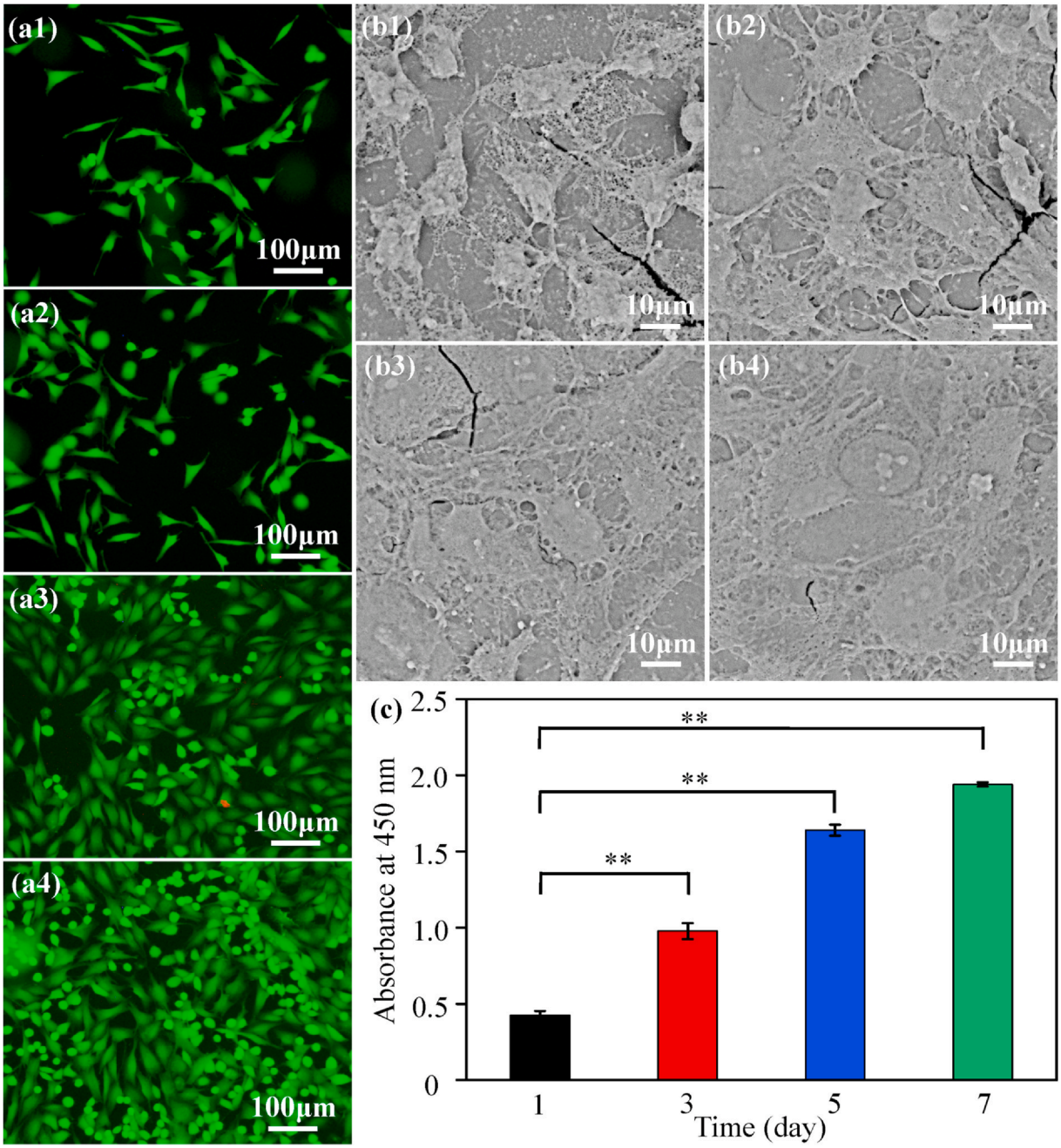

Fig. 8. Fluorescence images of cell skeletons on the 1PLLA/1PGA/HAP scaffold for (a1) 1 d, (a2) 3 d, (a3) 5 d and (a4) 7 d, SEM micrographs of cell morphology on the 1PLLA/1PGA/HAP scaffold for (b1) 1 d, (b2) 3 d, (b3) 5 d and (b4) 7 d, (c) Proliferation of cells on the 1PLLA/1PGA/HAP scaffold for different times (**$P < 0.01$). Data were presented as mean ± standard deviation.

the cytocompatibility of bone scaffold [56–58], and MG-63 cells were used for cell experiments in this study. Fluorescence images of MG-63 cells cultured on the 1PLLA/1PGA/HAP scaffold for 1, 3, 5 and 7 d were shown in Fig. 8(a1-a4). The results indicated that live cells were bright and well pronounced elongated filopodia, and a higher number of live cells were adhered to the scaffold on increasing days of cell culture time. Cell morphologies on the scaffold after different times of culture were shown in Fig. 8(b1-b4). The cells presented a polygonal morphology and spread well on the scaffold with interconnected filopodia. The number of lamellipodia and filopodia extensions from the cells was increased with progress in cell culture time. The proliferation of MG-63 cells on the scaffold was investigated using CCK-8 assay, and the results were presented in Fig. 8c. A increasing trend of cell proliferation was observed with progress in cell culture time, and the cell number at 3, 5 and 7 d were significantly higher than that at 1 d (**$P < 0.01$). These results suggested that the 1PLLA/1PGA/HAP scaffold had good cytocompatibility for cell adhesion, spreading and proliferation, which might be attributed to the presence of HAP in the scaffold. Studies had indicated that HAP was a natural bone mineral component, and the incorporation of HAP could provide a suitable environment for cell growth and proliferation.

In order to evaluate the bone regeneration ability, the 1PLLA/1PGA/HAP and PLLA/HAP scaffolds were implanted in the bone defect site whereas the blank group was used as control, and the results were presented in Fig. 9. All the rabbits survived during and after surgery, and no sign of inflammatory reactions and fractures were observed at the site of bone defect. Large blank region were observed in the blank group from the X-ray radiographs, demonstrating that there was a small

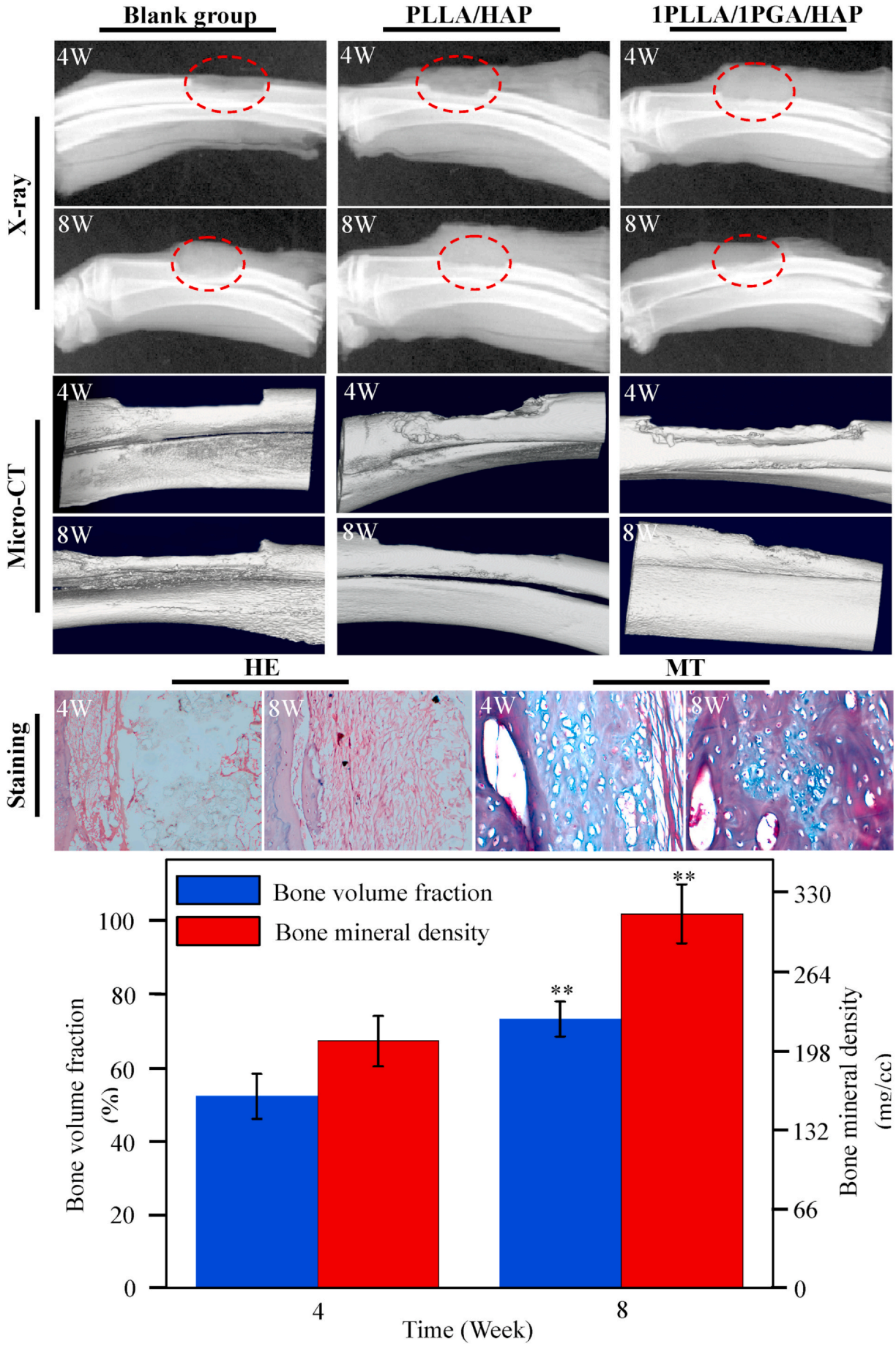

(caption on next page)

Fig. 9. X-ray radiographs and micro-CT images of the 1PLLA/1PGA/HAP scaffold, PLLA/HAP scaffold and blank group after 4 and 8 weeks implantation. HE and MT images, bone volume fraction and bone mineral density of the 1PLLA/1PGA/HAP scaffold after 4 and 8 weeks implantation (**P < 0.01). Data were presented as mean ± standard deviation.

amount of new bone formation. In the PLLA/HAP scaffold group, little radiopacity was observed around the defects at 4 weeks after the operation, and both ends of the bone defects were partially bridged at 8 weeks. Conversely, radio-opaque images were observed in the 1PLLA/1PGA/HAP scaffold group, demonstrating that considerable new bone formed in the defect region. The new bone tissue grew from the margin of defect toward the center, and both ends of defect region were partially bridged at 8 weeks. The 1PLLA/1PGA/HAP scaffold exhibited evidently more bone formation in the defect region compared to the PLLA/HAP scaffold and the blank group from the micro-CT images. Remarkably, no interfaces could be identified between the scaffold and the host bone after 8 weeks implantation, indicating that the 1PLLA/1PGA/HAP scaffold accelerated the mineralization of new bone tissue and promoted tissue integration.

Bone volume fraction and bone mineral density of the 1PLLA/1PGA/HAP scaffold at 8 weeks were extremely higher than that at 4 weeks in the quantitative analysis of micro-CT scanning (**$P < 0.01$). Histological examinations of new bone formation of the 1PLLA/1PGA/HAP scaffold were analyzed using HE and MT staining, and the results showed that there was a small amount of new bone tissues and fibrous tissues appeared in the defect region with the scaffold without any inflammatory response after 4 weeks. After 8 weeks, a large number of new bone tissue were observed accompanied by scaffold materials degraded, substantial osteoblasts and new vessels appeared. These indicated that the 1PLLA/1PGA/HAP scaffold could promote bone formation and bone defect repair. One possible reason for the good bone regeneration ability was the bioactivity and osteoconductivity of incorporated HAP. HAP nanoparticles exposed from the polymer matrix during the degradation of scaffold, and then provided an ideal microenvironment for osteoblasts growth and reproduction, thereby promoting new bone formation. Similar results were obtained when HAP was incorporated into PLGA scaffold, indicating that the incorporation of HAP into scaffold significantly enhanced the expressions of osteogenic differentiation-related genes, and the scaffold could provide satisfactory microenvironment for the regeneration of bone defect [59].

4. Conclusions

In the present study, biodegradable polymer PGA was blended into the HAP/PLLA scaffold to accelerate degradation so that the bioactivity and osteoconductivity could be fully displayed, and the composite scaffolds were fabricated by laser 3D printing technology. The results revealed that the incorporation of PGA could improve the hydrophilic of the scaffold with up-regulated water uptake capacity and the degradation rate by PGA degradation increasing the contact area between PLLA and body fluid. As a result, the embedded HAP exposed from the PLLA matrix, contacted and exchanged ions with body fluid, which facilitated bone like apatite deposition and then provided a suitable environment for osteoblastic growth and proliferation. *In vivo* bone defect repair experiments revealed that the PLLA/PGA/HAP scaffold could effectively support new bone tissue and blood vessel tissue growth, while the blank group had little effect on diminishing the bone defect area. In a word, the PLLA/PGA/HAP scaffold possess desirable biodegradability, bioactivity and osteogenesis ability, and hold great potential for bone tissue engineering application.

Declaration of interests

The authors declare that they have no known competing financial interests or personal relationships that could have appeared to influence the work reported in this paper.

Credit Author Statement

Cijun Shuai: Project administration, Formal analysis, Data curation, designed and discussed the project, performed the microstructural and mechanical tests, analyzed the data and wrote the manuscript. **Wenjing Yang:** Formal analysis, Data curation, Writing - original draft, performed the microstructural and mechanical tests, performed the biological experiments, analyzed the data and wrote the manuscript. **Pei Feng:** Project administration, Formal analysis, Writing - original draft, designed and discussed the project, performed the microstructural and mechanical tests, analyzed the data and wrote the manuscript. **Shuping Peng:** performed the microstructural and mechanical tests. **Hao Pan:** Writing - original draft, performed the biological experiments, All authors reviewed the manuscript.

Acknowledgements

This work was supported by the following funds: (1) The Natural Science Foundation of China (51905553, 51935014, 81871494, 81871498); (2) Hunan Provincial Natural Science Foundation of China (2019JJ50774, 2019JJ50588); (3) The Provincial Key R & D Projects of Jiangxi (20201BBE51012); (4) JiangXi Provincial Natural Science Foundation of China (20192ACB20005); (5) Guangdong Province Higher Vocational Colleges & Schools Pearl River Scholar Funded Scheme (2018); (6) The Project of Hunan Provincial Science and Technology Plan (2017RS3008); (7) The Project of State Key Laboratory of High Performance Complex Manufacturing, Central South University; (8) Shenzhen Science and Technology Plan Project (JCYJ20170817112445033).

References

[1] Y.Y. Zhou, S. Li, D.L. Wang, X. Han, X. Lei, Fabrication of collagen/HAP electrospun scaffolds with perfect HAP nanorods along nanofiber orientation, Sci. Adv. Mater. 10 (2018) 930–936.
[2] Q. Huang, Y. Liu, Z. Ouyang, Q. Feng, Comparing the regeneration potential between PLLA/Aragonite and PLLA/Vaterite pearl composite scaffolds in rabbit radius segmental bone defects, Bioact. Mater. 5 (2020) 980–989.
[3] J.Y. Kim, G. Ahn, C. Kim, J.S. Lee, I.G. Lee, S.H. An, et al., Synergistic effects of beta tri-calcium phosphate and porcine-derived decellularized bone extracellular matrix in 3D-printed polycaprolactone scaffold on bone regeneration, Macromol. Biosci. 18 (2018) 1800025.
[4] S. Lee, M.K. Joshi, A.P. Tiwari, B. Maharjan, K.S. Kim, Y.H. Yun, et al., Lactic acid assisted fabrication of bioactive three-dimensional PLLA/β-TCP fibrous scaffold for biomedical application, Chem. Eng. J. 347 (2018) 771–781.
[5] W. Yang, Y. Zhong, C. He, S. Peng, Y. Yang, F. Qi, et al., Electrostatic self-assembly of pFe_3O_4 nanoparticles on graphene oxide: a co-dispersed nanosystem reinforces PLLA scaffolds, J. Adv. Res. 24 (2020) 191–203.
[6] K. Liu, W. Li, S. Chen, W. Wen, L. Lu, M. Liu, et al., The design, fabrication and evaluation of 3D printed gHNTs/gMgO whiskers/PLLA composite scaffold with honeycomb microstructure for bone tissue engineering, Compos. B Eng. 192 (2020) 108001.
[7] S. Subramaniam, Y.H. Fang, S. Sivasubramanian, F.H. Lin, C.P. Lin, Hydroxyapatite-calcium sulfate-hyaluronic acid composite encapsulated with collagenase as bone substitute for alveolar bone regeneration, Biomaterials 74 (2016) 99–108.
[8] G. Ruphuy, A. Saralegi, J. Lopes, M.M. Dias, M.F. Barreiro, Spray drying as a viable process to produce nano-hydroxyapatite/chitosan (n-HAp/CS) hybrid microparticles mimicking bone composition, Adv. Powder Technol. 27 (2016) 575–583.
[9] S.M. Taromsari, M. Salari, R. Bagheri, M.A.F. Sani, Optimizing tribological, tensile & in-vitro biofunctional properties of UHMWPE based nanocomposites with simultaneous incorporation of graphene nanoplatelets (GNP) & hydroxyapatite (HAp) via a facile approach for biomedical applications, Compos. B Eng. 175 (2019) 107181.
[10] Z. Dong, Q. Yang, M. Mei, L. Liu, J. Sun, L. Zhao, et al., Preparation and characterization of fluoride calcium silicate composites with multi-biofunction for clinical application in dentistry, Compos. B Eng. 143 (2018) 243–249.
[11] M.D. Vlad, E.F. Aguado, S.G. González, I.C. Ivanov, E.V. Şindilar, I. Poeată, et al., Novel titanium-apatite hybrid scaffolds with spongy bone-like micro architecture intended for spinal application: in vitro and in vivo study, Mater. Sci. Eng. C-Mater. 110 (2020) 110658.

[12] N. Nezafati, M. Farokhi, M. Heydari, S. Hesaraki, N.A. Nasab, In vitro bioactivity and cytocompatablity of an injectable calcium phosphate cement/silanated gelatin microsphere composite bone cement, Compos. B Eng. 175 (2019) 107146.

[13] D. Beibei, F. Tiantang, L. Jiafeng, G. Li, Z. Qin, Y. Wuyou, et al., PLLA-grafted gelatin amphiphilic copolymer and its self-assembled nano carrier for anticancer drug delivery, Macromol. Chem. Phys. 220 (2019) 1800528.

[14] C.O. Goulart, F.R.P. Lopes, Z.O. Monte, J.S.V. Dantas, A. Souto, J.T. Oliveira, et al., Evaluation of biodegradable polymer conduits-poly (L-lactic acid)-for guiding sciatic nerve regeneration in mice, Methods 99 (2016) 28–36.

[15] R.W.N. Nugroho, K. Odelius, A. Höglund, A.C. Albertsson, The nature of polymer grafts and substrate shape on the surface degradation of poly (l-lactide), J. Appl. Polym. Sci. 132 (2015) 42736.

[16] X. Liu, P.X. Ma, The nanofibrous architecture of poly (L-lactic acid)-based functional copolymers, Biomaterials 31 (2010) 259–269.

[17] Z. Wang, Y. Wang, Y. Ito, P. Zhang, X. Chen, A comparative study on the in vivo degradation of poly (L-lactide) based composite implants for bone fracture fixation, Sci. Rep-UK 6 (2016) 1–12.

[18] S. Castillejos, J. Cerna, F. Meléndez, M.E. Castro, R. Aguilar, C. Márquez-Beltrán, et al., Bulk modification of poly (lactide)(PLA) via copolymerization with poly (propylene glycol) diglycidylether (PPGDGE), Polymers 10 (2018) 1184.

[19] C. Shuai, G. Liu, Y. Yang, F. Qi, S. Peng, W. Yang, C. He, G. Wang, G. Qian, A strawberry-like Ag-decorated barium titanate enhances piezoelectric and antibacterial activities of polymer scaffold, Nanomater. Energy 74 (2020) 104825.

[20] N. Iqbal, A.S. Khan, A. Asif, M. Yar, J.W. Haycock, I.U. Rehman, Recent concepts in biodegradable polymers for tissue engineering paradigms: a critical review, Int. Mater. Rev. 64 (2019) 91–126.

[21] M. Ayyoob, X. Yang, H.J. Park, S.Y. Park, J.H. Kim, S.W. Nam, et al., Synthesis of bioresorbable poly (Lactic-co-Glycolic acid) s through direct polycondensation: an economical substitute for the synthesis of polyglactin via ROP of lactide and glycolide, fiber, Polymer 20 (2019) 887–895.

[22] J.T.K. Thevar, N.A.N.N. Malek, M.R.A. Kadir, In vitro degradation of triple layered poly (lactic-co-glycolic acid) composite membrane composed of nanoapatite and lauric acid for guided bone regeneration applications, Mater. Chem. Phys. 221 (2019) 501–514.

[23] C. Shuai, L. Yu, P. Feng, Y. Zhong, Z. Zhao, Z. Chen, et al., Organic montmorillonite produced interlayer locking effect in polymer scaffold to enhance interfacial bonding, Mater. Chem. Front. 4 (2020) 2398–2408.

[24] Y. Yang, C. Lu, S. Peng, L. Shen, D. Wang, F. Qi, et al., Laser additive manufacturing of Mg-based composite with improved degradation behaviour, Virtual Phys. Prototyp. (2020) 1–16.

[25] C. Shuai, L. Yu, P. Feng, C. Gao, S. Peng, Interfacial reinforcement in bioceramic/biopolymer composite bone scaffold: the role of coupling agent, Colloids Surf., B 193 (2020) 111083.

[26] S. Toosi, H. Naderi-Meshkin, F. Kalalinia, M.T. Peivandi, H. HosseinKhani, A.R. Bahrami, et al., PGA-incorporated collagen: toward a biodegradable composite scaffold for bone-tissue engineering, J. Biomed. Mater. Res. 104 (2016) 2020–2028.

[27] S. Buyuksungur, T.E. Tanir, A. Buyuksungur, E.I. Bektas, G.T. Kose, D. Yucel, et al., 3D printed poly (ε-caprolactone) scaffolds modified with hydroxyapatite and poly (propylene fumarate) and their effects on the healing of rabbit femur defects, Biomater. Sci. 5 (2017) 2144–2158.

[28] C. Shuai, B. Wang, S. Bin, S. Peng, C. Gao, TiO_2 induced in situ reaction in graphene oxide reinforced AZ61 biocomposites to enhance the interfacial bonding, ACS Appl. Mater. Interfaces 12 (2020) 23464–23473.

[29] C. Shuai, S. Li, W. Yang, Y. Yang, Y. Deng, C. Gao, MnO_2 catalysis of oxygen reduction to accelerate the degradation of Fe-C composites for biomedical applications, Corrosion Sci. 170 (2020) 108679.

[30] W.L. Ng, C.K. Chua, Y.F. Shen, Print me an organ! Why we are not there yet, Prog. Polym. Sci. 97 (2019) 101145.

[31] C. Wang, W. Huang, Y. Zhou, L. He, Z. He, Z. Chen, X. He, S. Tian, J. Liao, B. Lu, Y. Wei, M. Wang, 3D printing of bone tissue engineering scaffolds, Bioact. Mater. 5 (2020) 82–91.

[32] P. Zhuang, A.X. Sun, J. An, C.K. Chua, S.Y. Chew, 3D neural tissue models: from spheroids to bioprinting, Biomaterials 154 (2018) 113–133.

[33] H. Golzar, D. Mohammadrezaei, A. Yadegari, M. Rasoulianboroujeni, M. Hashemi, M. Omidi, et al., Incorporation of functionalized reduced graphene oxide/magnesium nanohybrid to enhance the osteoinductivity capability of 3D printed calcium phosphate-based scaffolds, Compos. B Eng. 185 (2020) 107749.

[34] H. Jeon, M. Lee, S. Yun, D. Kang, K.H. Park, S. Choi, et al., Fabrication and characterization of 3D-printed biocomposite scaffolds based on PCL and silanated silica particles for bone tissue regeneration, Chem. Eng. J. 360 (2019) 519–530.

[35] T. Kuang, F. Chen, L. Chang, Y. Zhao, D. Fu, X. Gong, et al., Facile preparation of open-cellular porous poly (l-lactic acid) scaffold by supercritical carbon dioxide foaming for potential tissue engineering applications, Chem. Eng. J. 307 (2017) 1017–1025.

[36] C. Huang, S. Bhagia, N. Hao, X. Meng, L. Liang, Q. Yong, et al., Biomimetic composite scaffold from an in situ hydroxyapatite coating on cellulose nanocrystals, RSC Adv. 9 (2019) 5786–5793.

[37] W. Luo, L. Cheng, C. Yuan, Z. Wu, G. Yuan, M. Hou, et al., Preparation, characterization and evaluation of cellulose nanocrystal/poly (lactic acid) in situ nanocomposite scaffolds for tissue engineering, Int. J. Biol. Macromol. 134 (2019) 469–479.

[38] S. Milovanovic, D. Markovic, A. Mrakovic, R. Kuska, I. Zizovic, S. Frerich, et al., Supercritical CO2-assisted production of PLA and PLGA foams for controlled thymol release, Mater. Sci. Eng. C-Mater. 99 (2019) 394–404.

[39] S. Hassanajili, A. Karami-Pour, A. Oryan, T. Talaei-Khozani, Preparation and characterization of PLA/PCL/HA composite scaffolds using indirect 3D printing for bone tissue engineering, Mater. Sci. Eng. C-Mater. 104 (2019) 109960.

[40] Y. Lai, Y. Li, H. Cao, J. Long, X. Wang, L. Li, et al., Osteogenic magnesium incorporated into PLGA/TCP porous scaffold by 3D printing for repairing challenging bone defect, Biomaterials 197 (2019) 207–219.

[41] G. Liu, M. Fu, F. Li, W. Fu, Z. Zhao, H. Xia, et al., Tissue-engineered PLLA/gelatine nanofibrous scaffold promoting the phenotypic expression of epithelial and smooth muscle cells for urethral reconstruction, Mater. Sci. Eng. C-Mater. 111 (2020) 110810.

[42] M. Ayyoob, Y.J. Kim, Effect of chemical composition variant and oxygen plasma treatments on the wettability of PLGA thin films, synthesized by direct copolycondensation, Polymers 10 (2018) 1132.

[43] E. Aydin, J.A. Planell, V. Hasirci, Hydroxyapatite nanorod-reinforced biodegradable poly (L-lactic acid) composites for bone plate applications, J. Mater. Sci. Mater. Med. 22 (2011) 2413–2427.

[44] Y.F. Tang, J.G. Liu, Z.L. Wang, Y. Wang, L.G. Cui, P.B. Zhang, et al., In vivo degradation behavior of porous composite scaffolds of poly (lactide-co-glycolide) and nano-hydroxyapatite surface grafted with poly (L-lactide), Chin. J. Polym. Sci. 32 (2014) 805–816.

[45] A. Naik, D.V. Shepherd, J.H. Shepherd, S.M. Best, R.E. Cameron, The effect of the type of HA on the degradation of PLGA/HA composites, Mater. Sci. Eng. C-Mater. 70 (2017) 824–831.

[46] M.L. Zhao, G. Sui, X.L. Deng, J.G. Lu, S.K. Ryu, X.P. Yang, PLLA/HA electrospin hybrid nanofiber scaffolds: morphology, in vitro degradation and cell culture potential, Adv. Mater. Res. 11 (2006) 243–246.

[47] Y. Zhang, J. Wang, Y. Ma, B. Han, X. Niu, J. Liu, et al., Preparation of poly (lactic acid)/sintered hydroxyapatite composite biomaterial by supercritical CO_2, Bio Med. Mater. Eng. 29 (2018) 67–79.

[48] P. Feng, P. Wu, C. Gao, Y. Yang, W. Guo, W. Yang, et al., A multimaterial scaffold with tunable properties: toward bone tissue repair, Adv. Sci. 5 (2018) 1700817.

[49] C. Zhou, X. Ye, Y. Fan, L. Ma, Y. Tan, F. Qing, et al., Biomimetic fabrication of a three-level hierarchical calcium phosphate/collagen/hydroxyapatite scaffold for bone tissue engineering, Biofabrication 6 (2014) 035013.

[50] A.I. Martín, A.J. Salinas, M. Vallet-Regí, Bioactive and degradable organic-inorganic hybrids, J. Eur. Ceram. Soc. 25 (2005) 3533–3538.

[51] J. Lu, H. Yu, C. Chen, Biological properties of calcium phosphate biomaterials for bone repair: a review, RSC Adv. 8 (2018) 2015–2033.

[52] T. Tian, W. Xie, W. Gao, G. Wang, L. Zeng, G. Miao, et al., Micro-nano bioactive glass particles incorporated porous scaffold for promoting osteogenesis and angiogenesis in vitro, Front. Chem. 7 (2019) 186.

[53] D.A. Sánchez-Téllez, L. Téllez-Jurado, L.M. Rodríguez-Lorenzo, M.A. Mazo, J. Rubio, A. Tamayo, Surface effects on the degradation mechanism of bioactive PDMS-SiO_2-CaO-P_2O_5 hybrid materials intended for bone regeneration, Ceram. Int. 43 (2017) 476–483.

[54] M. Xu, F. Ji, Z. Qin, D. Dong, X. Tian, R. Niu, et al., Biomimetic mineralization of a hydroxyapatite crystal in the presence of a zwitterionic polymer, CrystEngComm 20 (2018) 2374–2383.

[55] L. Cao, W. Liu, Y. Zhong, Y. Zhang, D. Gao, T. He, et al., Linc 02349 promotes osteogenesis of human umbilical cord-derived stem cells by acting as a competing endogenous RNA for miR-25-3p and miR-33b-5p, Cell Prolif 53 (2020) e12814.

[56] S. He, S. Yang, Y. Zhang, X. Li, D. Gao, Y. Zhong, et al., LncRNA ODIR1 inhibits osteogenic differentiation of hUC-MSCs through the FBXO25/H2BK120ub/H3K4me3/OSX axis, Cell Death Dis. 10 (2019) 1–16.

[57] Z. Zou, W. Liu, L. Cao, Y. Liu, T. He, S. Peng, et al., Advances in the occurrence and biotherapy of osteoporosis, Biochem. Soc. Trans. (2020) BST20200005.

[58] Y. Yang, S. Yang, Y. Wang, Z. Yu, H. Ao, H. Zhang, et al., Anti-infective efficacy, cytocompatibility and biocompatibility of a 3D-printed osteoconductive composite scaffold functionalized with quaternized chitosan, Acta Biomater. 46 (2016) 112–128.